SCIENTIFIC REPORTS

OPEN

SUBJECT AREAS:
ELECTRONIC DEVICES
ATOMISTIC MODELS
THERMODYNAMICS

Received
16 October 2013

Accepted
5 February 2014

Published
24 February 2014

Correspondence and requests for materials should be addressed to S.-Y.C. (shouyi@dragon.nchu.edu.tw)

Structural and Thermodynamic Factors of Suppressed Interdiffusion Kinetics in Multi-component High-entropy Materials

Shou-Yi Chang[1], Chen-En Li[1], Yi-Chung Huang[1], Hsun-Feng Hsu[1], Jien-Wei Yeh[2] & Su-Jien Lin[2]

[1]Department of Materials Science and Engineering, National Chung Hsing University, Taichung 40227, Taiwan, [2]Department of Materials Science and Engineering, National Tsing Hua University, Hsinchu 30013, Taiwan.

We report multi-component high-entropy materials as extraordinarily robust diffusion barriers and clarify the highly suppressed interdiffusion kinetics in the multi-component materials from structural and thermodynamic perspectives. The failures of six alloy barriers with different numbers of elements, from unitary Ti to senary TiTaCrZrAlRu, against the interdiffusion of Cu and Si were characterized, and experimental results indicated that, with more elements incorporated, the failure temperature of the barriers increased from 550 to 900°C. The activation energy of Cu diffusion through the alloy barriers was determined to increase from 110 to 163 kJ/mole. Mechanistic analyses suggest that, structurally, severe lattice distortion strains and a high packing density caused by different atom sizes, and, thermodynamically, a strengthened cohesion provide a total increase of 55 kJ/mole in the activation energy of substitutional Cu diffusion, and are believed to be the dominant factors of suppressed interdiffusion kinetics through the multi-component barrier materials.

In 2004, Yeh reported a brand-new concept of alloy design, named high-entropy alloys (HEAs), with equimolar incorporations of multi-principal (more than five) metallic elements[1]. Thermodynamically, owing to high mixing entropies, simple solid-solution structures rather than any complex phases or intermetallics are typically formed in HEAs[2,3]; structurally and kinetically, severe lattice distortions caused by different atom sizes suppress diffusion and nucleation/growth rates, generally yielding nanocrystalline or even amorphous structures[4]. In the past years, HEAs have been intensively studied, and many extraordinary properties including a good mechanical performance[5], a unique elasticity[6], high plasticity[7], and high saturation magnetization and electrical resistivity[8] been discovered. Films of HEA nitrides (HEANs), such as (AlCrTaTiZr)N, with simple solid-solution or nanocomposite structures and very good mechanical properties (high hardness and wear resistance) were afterwards developed as protective hard coatings[9,10]. Attributed to their high thermal stability, thin HEA and HEAN layers have also been considered for further applications to diffusion barriers[11]. Robust diffusion barriers are of importance for use as interfacial layers particularly in the interconnects of integrated circuits (ICs), e.g. between Cu wires and dielectrics or between metal pads and solders, to inhibit the interdiffusion of adjacent materials and the formation of compounds (e.g. silicides)[12]. Refractory transition metals, such as Ti and Ta[12], and the nitrides of unitary transition metals, including TiN and TaN of strong ionic bonds[13,14], were first developed and practically used in interconnects, but however unsuited for applications to next-generation interconnects due to their high solid solubility to Cu and their columnar structures with boundaries as fast diffusion paths. Thinner and more effective barriers have been investigated in recent years, which typically comprise: (1) ternary components with an amorphous structure to diminish diffusion paths, such as Ru-Ti-N and Ru-Ta-N[15–17], or (2) layered structures with interface mismatches to elongate diffusion paths, such as Ru/TaN and Ru/TaCN[18–20]. Nevertheless, in the IC manufacturing generation below 20 nm, robust and ultrathin barrier layers ($<$3 nm) with a high diffusion resistance are strongly demanded but rarely reported. Though self-forming (barrier-less alloy) and self-assembled (organic monolayer) diffusion barriers have been developed in the past few years[21,22], their thermal stability is yet concerned.

Recent studies indicated that, by the multi-component-induced lattice distortions and the layered structure-caused interface mismatches, HEA and HEAN barriers such as senary AlCrRuTaTiZr and (AlCrRuTaTiZr)N and their stacking structures with a thickness down to only 4 nm presented an extreme resistance to the interdiffusion of Cu and Si[23–26]. Their high endurance temperature (almost 900°C) against interdiffusion suggests the high potential of HEAs and HEANs as very promising barriers for practical applications to Cu interconnects.

SCIENTIFIC REPORTS SREP-13-04973.3d 12/2/14 14:00:58

Unfortunately, except a general concept of "lattice distortions", not an exact mechanism why HEAs and HEANs provide a high resistance to interdiffusion has been established. An amorphous structure is not simply the answer because thin sputtered Ti and TiN films are also possibly amorphous but do not present such a high resistance. The question remains. Hence in this study, six alloy films with different numbers of metallic elements (nA), from unitary Ti (1A), binary TiTa (2A), ternary TiTaCr (3A), quaternary TiTaCrZr (4A), quinary TiTaCrZrAl (5A) to senary TiTaCrZrAlRu (6A) (element added following the development sequence of diffusion barriers), were prepared and characterized; the resistance of ultrathin alloy diffusion barrier layers (DB_{nA}, ~7 nm thick) to the interdiffusion of Cu and Si (in term of the failures of Si/DB_{nA}/Cu film stacks), along with the interdiffusion kinetics through the alloy barriers, were determined to examine the enhanced resistant ability with more metallic elements incorporated. Mechanistic studies of structural and thermodynamic factors, from the aspects of lattice distortion, cohesive energy and packing density, were also performed to clarify the suppressed interdiffusion kinetics in multi-component high-entropy alloys.

Results

Compositions and structures. Compositional and structural analyses, as shown in Figure 1, indicate the uniform and simple solid-solution structures of the six alloy films investigated in the present study. From the elemental contents of the as-deposited thick alloy (nA) films given in Figure 1 (a), it was known that the metallic elements added in the alloys were in near-equimolar ratios, only except that in the binary alloy the Ta content was unexpectedly higher than Ti (Ta : Ti ~ 3 : 1) due to the resputtering of the light Ti compared to the heavy Ta. A few content (~3 at.%) of oxygen existed owing to the limited vacuum of the sputtering chamber. Although the elemental contents of the thick alloy films do not certainly equal to the compositions of thin diffusion barrier layers because they may slightly vary with film thickness, the measured data are still believed to represent the good composition uniformity of the thin layers. The XRD pattern of each thick alloy film in Figure 1 (b) presented only one set of peaks, revealing the simple solid-solution structures of the alloys even with the additions of multiple components. For the unitary alloy, main diffraction peaks at 2θ = 35.0°, 38.3° and 40.1° (corresponding to the (100), (002) and (101) lattice planes of Ti; JCPDS #44-1294) indicated a hexagonal close-packed (hcp) crystal structure, while for the binary alloy, the peaks at 38.4°, 55.2° and 69.5° (to (110), (200) and (211) planes) differently suggested a body-centered cubic (bcc) structure because a large portion of bcc Ta (JCPDS #04-0788) was added. In comparison for the ternary to senary alloys, broad hills, rather than sharp peaks, were observed, indicating the appearance of amorphous structure. Nevertheless, the positions (2θ) of the hill tops around 38.5–40.5° and 69.8–70.9° ($\sin\theta$ ratio ~ $1 : \sqrt{3}$) well accorded with the (110) and (211) peaks of bcc structure, suggesting a tendency of forming a bcc-based, short-range-ordered structure (embedded in the amorphous matrix) in these alloys. Peak shifts were noticed, which accorded with the variations in the average atom sizes (following the Bragg law) of the alloys with more metallic elements incorporated, as listed in Supplemental Table S1.

Diffusion resistance. The resistance of thin barrier layers (DB_{nA}) with different numbers of metallic elements to the interdiffusion of Cu and Si is determined from the failures of the Si/DB_{nA}/Cu film stacks, which are characterized from SEM morphologies, XRD patterns, electrical resistivities, and also TEM microstructures before and after thermal annealing, as presented in Figures 2 to 6. Figure 2 first shows the SEM morphologies of the as-deposited and thermally annealed Si/DB_{nA}/Cu stacks. As the annealing temperature increased to the endurance limits where the diffusion barriers still resist obvious interdiffusion of Cu and Si, the grains of the top Cu films grew, accompanied by slight Cu agglomerations to form voids or even islands (in particular for the Si/DB_{1A}/Cu stack at 500°C and Si/DB_{2A}/Cu at 600°C), but still exhibited smooth surfaces. The stacks failed at extreme temperatures (defined as the failure temperatures) once Cu penetrated through the barrier layers into and reacted with Si to form typical particulate-like Cu silicides. With more metallic elements incorporated in the alloy barriers, clearly, the failure temperature increased from 600 to 900°C.

The XRD patterns and electrical resistivities of the as-deposited and thermally annealed Si/DB_{nA}/Cu stacks, as plotted in Figures 3 (a) and (b), respectively, showed the same failure trend with the number of metallic elements. In the XRD pattern of the as-deposited stacks, a slightly broad peak at 43.3° corresponded to the (111) lattice plane of face-centered cubic (fcc) Cu with a fine grain size. For the annealed stacks at the endurance limits, the Cu (111) peaks sharpened because of grain growth, while at their failure temperatures, two additional peaks at 44.7° and 45.3° corresponding to the (320) and (312) lattice planes of typical Cu_3Si compound appeared, revealing the severe interdiffusion of Cu and Si. The formation of Cu silicides led to consequent drastic increases in the electrical resistivities of the failed stacks. Originally, high electrical resistivities of the as-deposited stacks were measured, above 10 μΩ-cm, due to the defects in the Cu films. With thermal annealing till the endurance limits, the

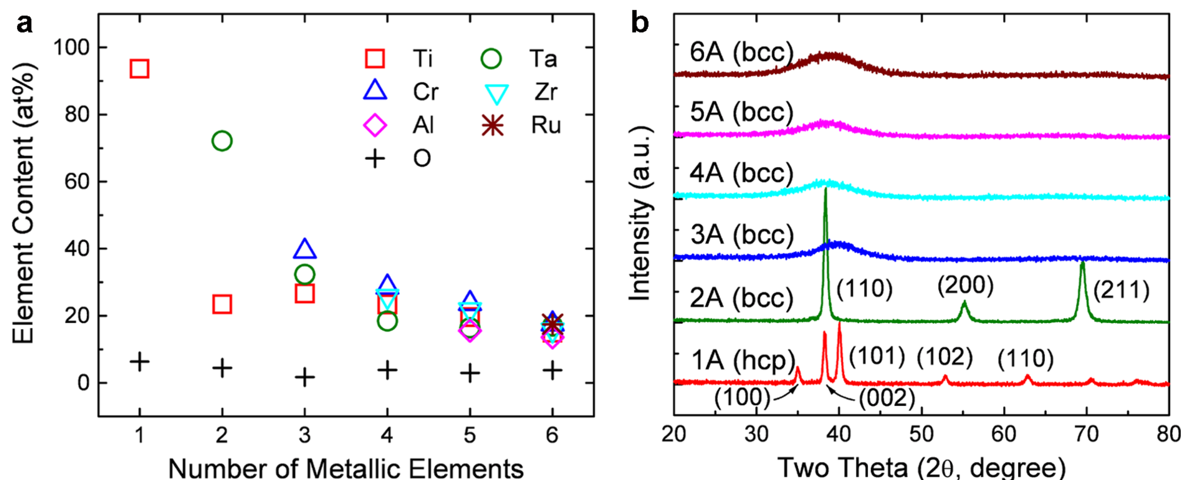

Figure 1 | (a) Elemental contents and (b) XRD patterns of as-deposited thick nA alloy films (n: number of metallic elements; hcp: hexagonal close-packed, bcc: body-centered cubic).

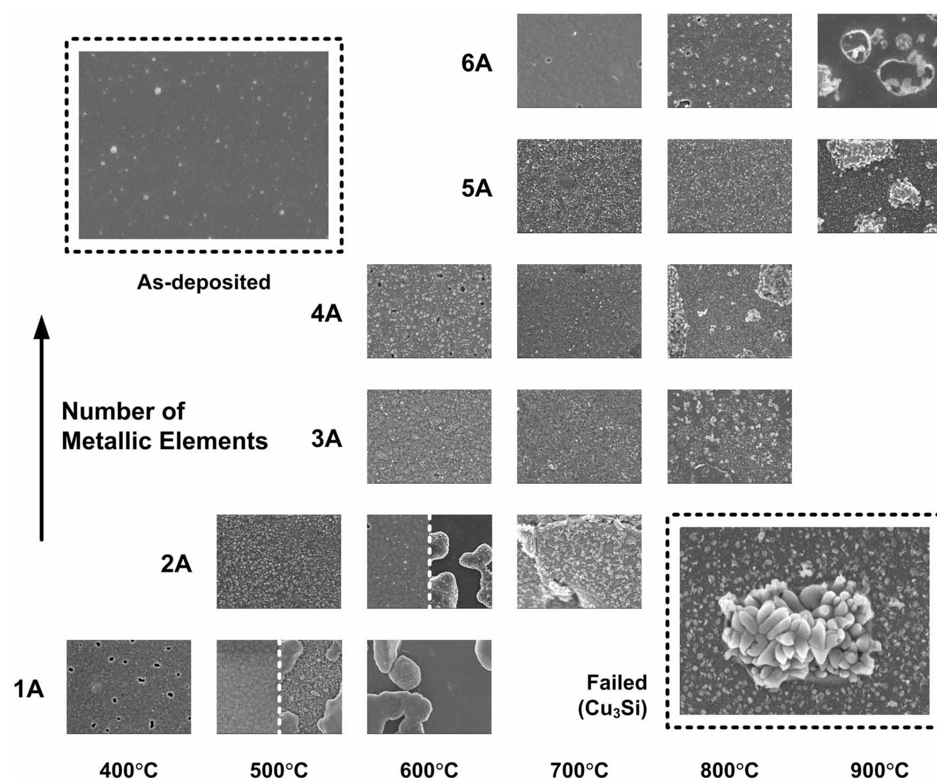

Figure 2 | SEM surface morphologies of as-deposited and thermally annealed Si/DB_{nA}/Cu film stacks (*n*: number of metallic elements; Cu film agglomerations into islands on the film stacks with DB_{1A} at 500°C and DB_{2A} at 600°C); insets: (up left) as-deposited with a typical Cu film surface, (down right) failed with a typical silicide formation.

electrical resistivities gradually decreased to only 2.5 μΩ-cm, close to the value of pure Cu, owing to Cu grain growth and defect eliminations. Then at the failure temperatures (600 to 900°C for Si/DB_{1A}/Cu to Si/DB_{6A}/Cu respectively), a jump in resistivity to a high value occurred as a consequence of the abundant formation of Cu silicides (note: the resistivities of some regions on Si/DB_{1A}/Cu and Si/DB_{2A}/Cu stacks early jumped at 500 and 600°C, respectively, owing to Cu agglomerations to discontinuous islands). In comparison, Si/Cu without a barrier failed very early at 400–500°C similar to the reported temperature[16].

The above analyses verified that the Si/DB_{1A}/Cu film stack completely failed at 600°C, while Si/DB_{6A}/Cu did not until 900°C. However, it was noted that, by careful examinations of magnified SEM morphologies, XRD patterns and electrical resistivities (Supplemental Figure S1), the Si/DB_{1A}/Cu and Si/DB_{5A}/Cu stacks might have possibly failed at 500–600°C and 800–900°C, respectively, because very small compound particles formed, very low (320) and (312) peaks of silicides appeared, and electrical resistivities slightly rose. As plotted in Figure 4, it is concluded that the failure temperature of the film stacks, namely the diffusion resistance of the barriers, increased with the number of incorporated metallic elements, from 500–600°C (noted as 550°C) for the unitary, 700°C for the binary, 800°C for the ternary and quaternary, 800–900°C (850°C) for the quinary, to 900°C for the senary alloy.

The TEM cross-sectional microstructures and lattice images of the as-deposited and the 400–600°C annealed Si/DB_{1A}/Cu and 700–900°C annealed Si/DB_{6A}/Cu film stacks shown in Figure 5 confirmed the markedly enhanced diffusion resistance of multi-component

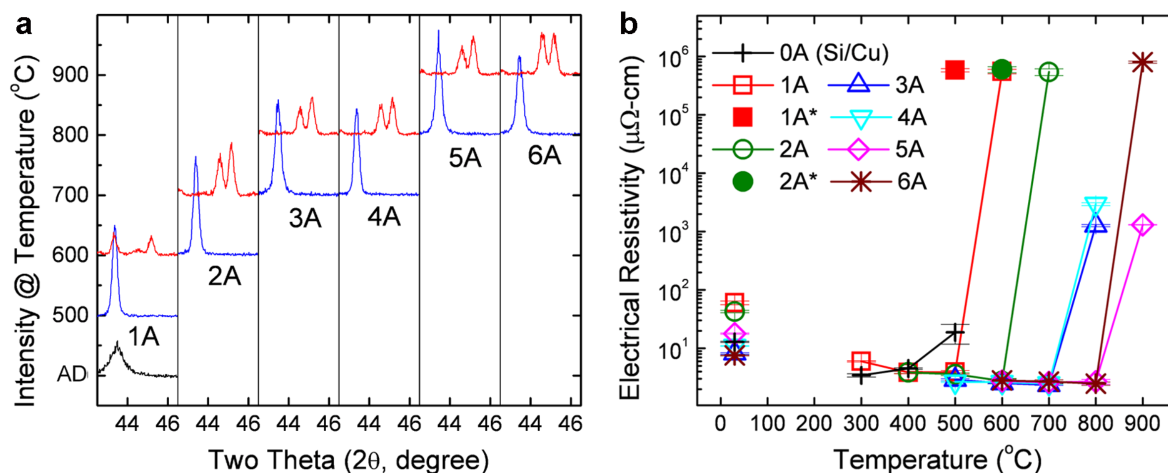

Figure 3 | (a) XRD patterns and (b) electrical resistivities of as-deposited and thermally annealed Si/DB_{nA}/Cu film stacks (*n*: number of metallic elements; AD: as-deposited; 0A: Si/Cu without a diffusion barrier; "*" following "1A" and "2A": Cu film agglomerations).

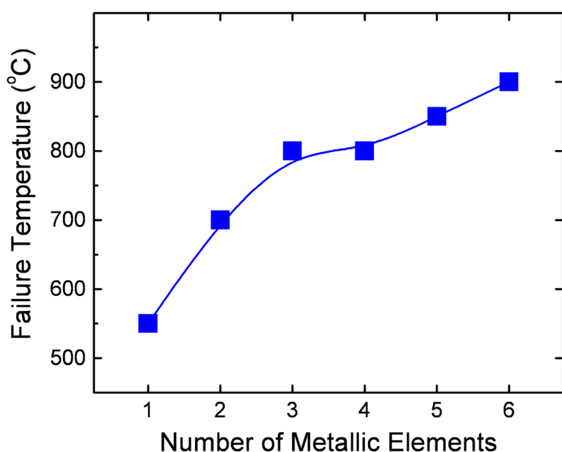

Figure 4 | **Failure temperatures of Si/DB$_{nA}$/Cu film stacks (*n*: number of metallic elements).**

alloys. In the as-deposited stacks, both the DB_{1A} and DB_{6A} layers of only 7 nm thick showed an amorphous structure, while the Si substrate and the Cu film (interplanar spacings 0.209 and 0.181 nm, (111) and (200) lattice planes; JCPDS # 85-1326) exhibited a crystalline, ordered structure. Between each two layers, a clear, continuous interface was identified. Compared to the thick unitary alloy film of a crystalline hcp structure and the thick senary alloy film of a bcc-based, short-range-ordered structure, the as-deposited ultrathin barrier layers more easily formed an amorphous structure[27,28]. However, a possibility should still be noted that a short-range ordering might exist in the amorphous (disordered) matrix[29], which needs to be further investigated. After annealing of Si/DB_{1A}/Cu at 400 to 500°C and Si/DB_{6A}/Cu at 700 to 800°C, clear interfaces and the amorphous structure of the alloy barriers basically remained despite few indistinct short-range orderings (several atomic layers in size) that might have possibly formed in the amorphous matrix of the 500°C-annealed DB_{1A} and the 800°C-annealed DB_{6A} layers. However, in the 500°C-annealed Si/DB_{1A}/Cu, few $CuTi_3$ nanocrystallites (interplanar spacing 0.227 nm, (114) plane; JCPDS #50-1476) were noticed, suggesting the interdiffusion of Cu and Ti as well as the beginning of failure. The Si/DB_{1A}/Cu completely failed at 600°C, and the Si/DB_{6A}/Cu did at 900°C; diffused interfaces and $CuTi_3$, $Cu_{15}Si_4$ (interplanar spacing 0.340 nm, (220) plane; JCPDS #76-1800) and Cu_5Si (interplanar spacing 0.280 nm, (210) plane; JCPDS #04-0841) nanocrystallites were found.

Activation energy of Cu diffusion. From Fick's second law[30], for non-static diffusion in a semi-infinite system which is similar to the interdiffusion of Cu and Si in Si/DB_{nA}/Cu film stacks through the thin alloy barrier layers, the concentration C of diffusing species as a function of distance x and time t, is given as $C=\frac{M}{\sqrt{\pi Dt}}\exp\left(-\frac{x^2}{4Dt}\right)$ where M and D are the thickness and diffusivity of the diffusing species, respectively, and the diffusion distance (at a constant concentration) is given as $x=2\sqrt{Dt}$. Accordingly, to determine the diffusion distances and diffusivities of Cu through the alloy barriers, the concentration distributions of Cu and Si elements in the as-deposited and thermally annealed Si/DB_{1A}/Cu and Si/DB_{6A}/Cu stacks at different temperatures were detected by TEM line scanning, as typically presented in Supplemental Figure S2. The curve fittings of the as-received data were performed using a sigmoid function to yield smooth elemental concentration profiles, as plotted in Figure 6 (the interfaces between the barriers and the native oxide were offset to zero in distance). Obviously, as temperature increased, Cu penetrated far into Si substrates through the alloy barriers. As presented in Figure 7 (a), the diffusion distances of Cu, at a fixed concentration of 50 at.%, in the annealed Si/DB_{1A}/Cu and Si/DB_{6A}/Cu stacks (referred to the as-deposited stacks) normally increased with temperature but decreased with the number of incorporated metallic elements. The diffusivities of Cu at different temperatures were further determined by using $x=2\sqrt{Dt}$, as plotted in Figure 7 (b) (vs. 1/temperature). In the Si/DB_{1A}/Cu stack the diffusivity of Cu reached 4.1×10^{-20} m^2/s at 600°C, while in the Si/DB_{6A}/Cu it was only 1.6×10^{-21} m^2/s at 700°C and 8.0×10^{-20} m^2/s at 900°C, obviously indicating the suppressed interdiffusion by the multi-component barriers.

From the experimentally measured logarithmic diffusivity-to-1/temperature relations in Figure 7 (b) and the equation $D=D_0\exp\left(-\frac{Q}{RT}\right)$ in which the diffusivity constant D_0 is a frequency factor, R the gas constant, and T the temperature[30], the activation energy of Cu diffusion in the Si/DB_{1A}/Cu and Si/DB_{6A}/Cu stacks, through the unitary and senary alloys, is then determined as 110 and 163 kJ/mol, respectively, as given in Figure 8. The increase in activation energy, 53 kJ/mol, yields a lowered diffusivity of Cu and

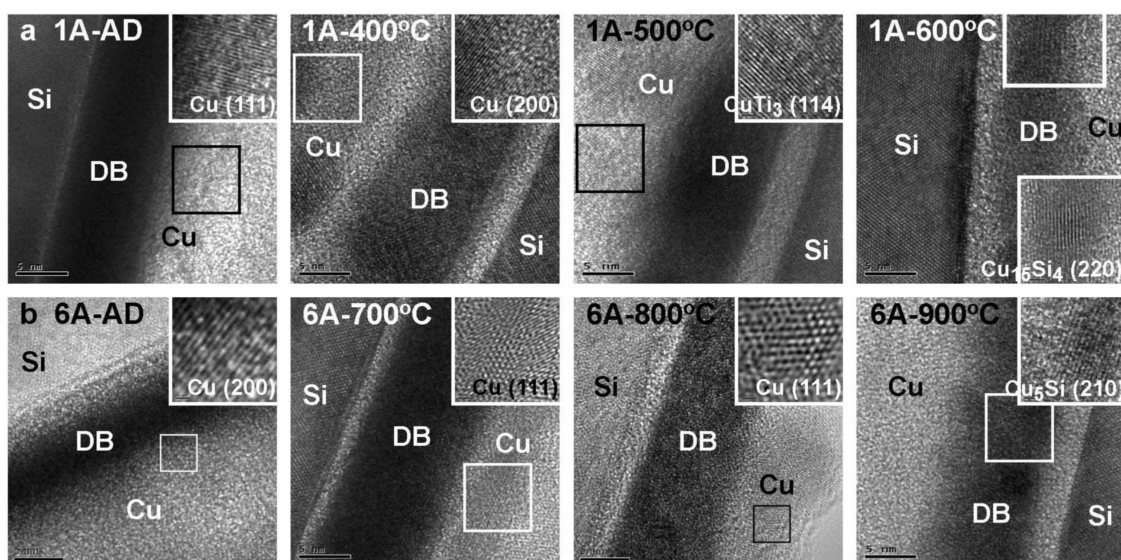

Figure 5 | TEM cross-sectional microstructures of as-deposited and thermally annealed Si/DB$_{nA}$/Cu film stacks (*n*: number of metallic elements) with (a) DB_{1A}, as-deposited and at 400–600°C, and (b) DB_{6A}, as-deposited and at 700–900°C (AD: as-deposited); insets: magnified lattice images.

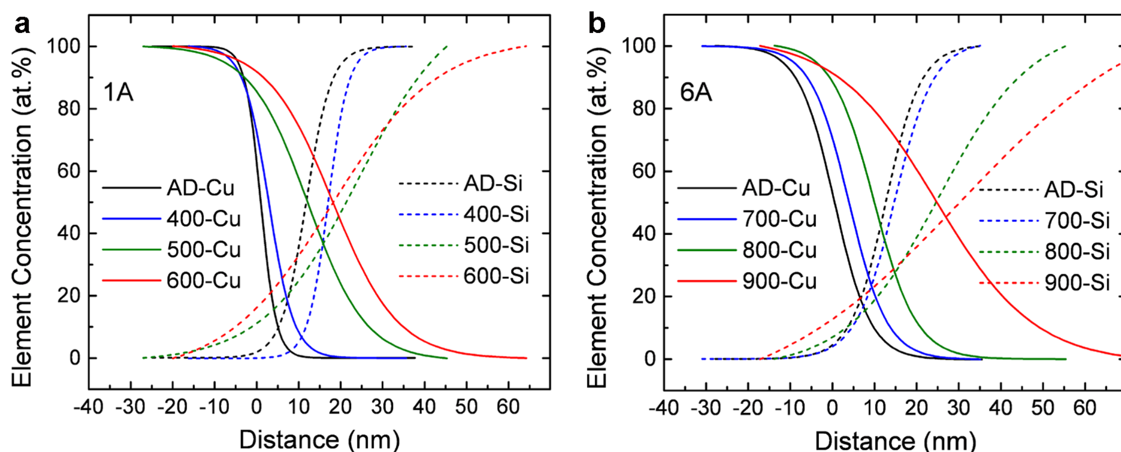

Figure 6 | Elemental concentration profiles of Cu and Si in as-deposited and thermally annealed Si/DB_{nA}/Cu film stacks (*n*: number of metallic elements) with (a) DB_{1A}, as-deposited and at 400–600°C, and (b) DB_{6A}, as-deposited and at 700–900°C (AD: as-deposited).

elucidates the markedly enhanced diffusion resistance of the senary alloys. Further according to the measured failure temperatures of Si/DB_{nA}/Cu stacks plotted in Figure 4, the activation energy of Cu diffusion through the binary to quinary alloys is proportionally interpolated, as also given in Figure 8 that clearly reflects the raised difficulty of Cu diffusion through the alloy barriers with more metallic elements incorporated.

Discussion

Several models for Cu diffusion in conventional barrier materials, established by using molecule dynamic simulations, have been reported[31–33], including the diffusion in metals via vacancies along different directions and that in nitrides via vacancies or interstitial sites. The model for diffusion in bcc Ta via vacancies suggests the smallest activation energy of diffusion along the [111] direction (0.65 eV, 63 kJ/mol), but higher energy along [100] (2.7 eV, 261 kJ/mol) and [110] (5.8 eV, 560 kJ/mol)[31]. In the present study, the similar-level but ascending activation energy with increasing the number of metallic elements is believed to reveal that Cu diffusion in the alloy barriers proceeds substitutionally via vacancies along the most facile direction but is possibly hindered by some factors discussed below. For the substitutional diffusion of atom from a lattice site to another, two requirements need to be fulfilled: (1) an adjacent vacancy (activation energy of vacancy formation, ΔG_f) and (2) a bond breaking and an atom transfer (activation energy of movement, ΔG_m), both of which compose the activation energy of diffusion[30]. Accordingly, three important factors for the increased activation energy of Cu diffusion, i.e. suppressed interdiffusion of Cu and Si, in the present multi-component alloy barriers are considered to be, structurally, the strain energy of lattice distortions and the packing density of atoms, and, thermodynamically, the cohesive energy of atoms, all of which concern vacancy formation and atom movement.

(1) Lattice distortion strain energy. Figure 9 (a) schematically illustrates the normal (regular, isotropic) lattice structure of unitary alloy and, differently, the distorted (atom displaced and/or bond shortened/stretched) structure of multi-component solid-solution alloy (random distribution with different atom sizes and cohesion with different bond strengths). In the unitary lattice with the same stress state in all directions, atoms diffuse via adjacent vacancies along the most facile direction (e.g. [111] in a bcc crystal) of the lowest energy barrier[31]. However, in the multi-component lattice with different stress distributions in different directions, the lattice strain energy is anticipated to influence the site of vacancy formation and the direction of atom movement; vacancies will form and atoms will migrate more frequently along more distorted directions (not certainly [111]). The total diffusion paths will be elongated, and the average difficulty in diffusion (i.e. the activation energy of diffusion) will increase, lowering the diffusivity of atoms in the multi-component alloys. The lattice distortions δ in

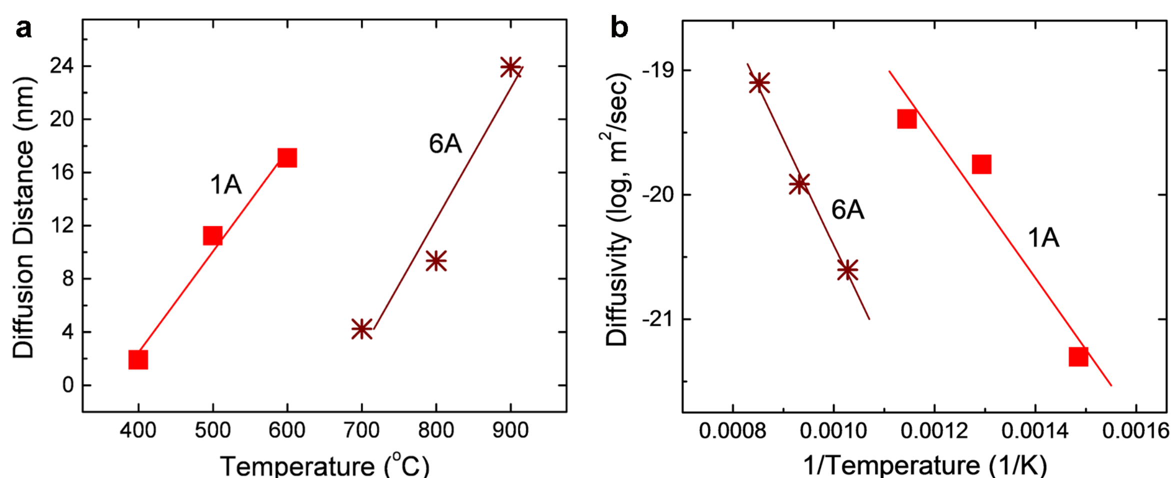

Figure 7 | (a) Diffusion distances and (b) diffusivities of Cu in thermally annealed Si/DB_{nA}/Cu film stacks (*n*: number of metallic elements) with DB_{1A} at 400–600°C and DB_{6A} at 700–900°C.

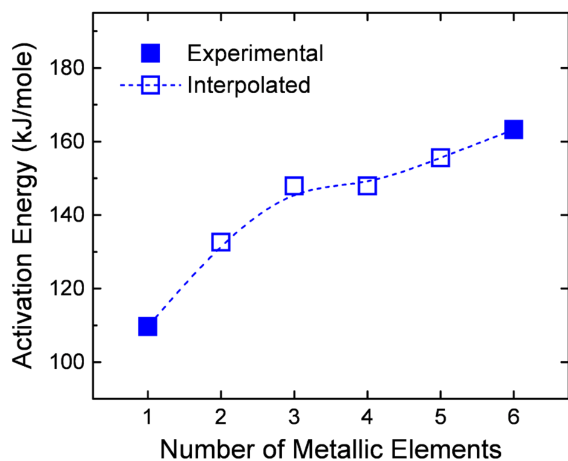

Figure 8 | Activity energy of Cu diffusion in Si/DB_{nA}/Cu film stacks (*n*: number of metallic elements; experimentally measured for the film stacks with DB_{1A} and DB_{6A}, interpolated for the film stacks with DB_{2A}–DB_{5A}).

the multi-component alloys can be calculated by using the equation $\delta=\sqrt{\sum_{i=1}^{n}X_i\left(1-\frac{r_i}{\bar{r}}\right)^2}$ in which X_i is the fraction of the *i*th component, and r_i and $\bar{r}$ the *i*th and the average atom radii, respectively[34]. The lattice distortion strain energy ΔU_{strain} is then theoretically calculated from the equation $\Delta U_{strain}=(\bar{E}\delta)(2\bar{r})^2\bar{d}$ where $\bar{E}$ is the average modulus (listed in Supplemental Table S1) and $\bar{d}$ the average displacement of atoms ($\bar{d}=\delta\bar{r}$), as plotted in Figure 9 (b) with the number of incorporated metallic elements. Compared to the zero energy of the unitary alloy without distortions, the lattice strain energy of the present multi-component alloys increases to 16.8 kJ/mol with four metallic elements and slightly decreases to 11.9 and 14.6 kJ/mol with five and six elements, respectively. The change in the electrical resistivities of thick alloy films, as given in Supplemental Figure S3, confirms the variation of lattice distortions with the number of metallic elements. Besides a typical film defect-caused increase in experimentally measured electrical resistivity from a theoretically calculated value (by the rule of mixture)[35], an extra increase (delta, relative to the typical increase of unitary alloy without lattice distortions) induced by lattice strains follows the variation trend of lattice distortions though a slight inconsistency exists for the quaternary and quinary alloys. The high lattice strain energy in the multi-component alloys with different-size atoms is also a dominant factor for the high stability of their amorphous structure in intense annealing, as suggested in Results that the temperature for the amorphous senary alloy to endure crystallization, 800°C, is much higher than that for the unitary alloy, only 500°C. Crystallization of multi-component alloys will cause much severer lattice distortions and higher lattice strain energy, while a topological instability will facilitate an amorphous solid solution, especially at high temperatures where an entropic force assists the formation and stabilization of solid-solution phases (random distributions of different-size atoms)[36].

(2) Cohesive energy. As also seen in Figure 9 (a), in the unitary lattice with the same cohesion between any adjacent atoms, atoms move via adjacent vacancies along the most facile direction[31]. In the multi-component lattice with anisotropic cohesions in different directions, however, high cohesive energy is expected to inhibit a bond breaking for vacancy formation and atom movement, and to change the direction of atom movement; vacancies will form and atoms will migrate more frequently along less strengthened directions. The average bond breaking energy will increase, the total diffusion paths will be elongated, and the average difficulty in diffusion (i.e.

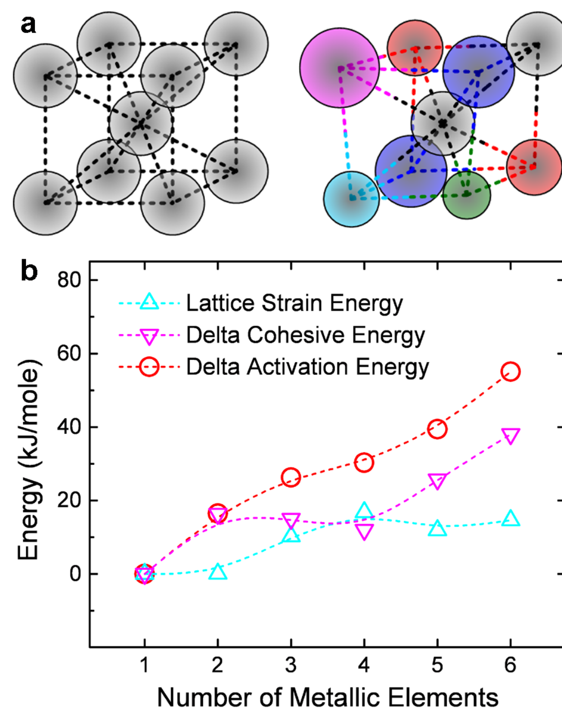

Figure 9 | (a) Schematic illustrations of normal unitary (left) and distorted multi-component solid-solution (right) lattice/bond structures; (b) theoretically calculated lattice distortion strain energy, increases in cohesive energy and total increases in the activation energy of Cu diffusion in/through *n*A alloys (*n*: number of metallic elements).

the activation energy of diffusion) will increase, then lowering the diffusivity of atoms in the multi-component alloys as well. Supplemental Table S2 lists the mixing enthalpies ΔH_{ij}^{mix} and cohesive energy Ω_{ij} of any two elements in the present multi-component alloys where the cohesive energy of the *i*th and *j*th components is obtained by Miedema's thermodynamic model $\Omega_{ij}=\frac{\Omega_{ii}+\Omega_{jj}}{2}-\Delta H_{ij}^{mix}$ [37–39]. From Takeuchi's regular-solution model $\Omega^{mix}=\sum_{i=1}^{n-1}\sum_{j=i+1}^{n}\Omega_{ij}X_iX_j$ [40], the cohesive energy Ω^{mix} of the present multi-component alloys is further theoretically calculated. Relative to the cohesive energy of the unitary alloy, 14.2 kJ/mol, the average increases in the cohesive energy, ΔH^{mix}, of the multi-component alloys are found to increase to 38.1 kJ/mol with the number of metallic elements, as plotted in Figure 9 (b).

(3) Packing density. The packing density of atoms in a unitary alloy with a bcc or fcc/hcp structure is 0.68 or 0.74, respectively. However, in a multi-component solid-solution alloy that is mixed with different-size atoms, the packing density will increase[41]. The shrinkage in free volume is believed to diminish vacancy formation/concentration, additionally increasing the difficulty in diffusion (i.e. the activation energy of diffusion) and lowering the diffusivity of atoms in the multi-component alloys. From Danisch's random-packing model of different-size balls[41], the packing densities of multi-component alloys with different coordination numbers and atom-size ratios ($\frac{r}{\bar{r}}1+\delta$, δ: lattice distortions) are theoretically calculated, as plotted in Supplemental Figure S4. For the hcp-based unitary alloy (with an atom-size ratio of 1), the packing density S is normally 0.740, while for the bcc-based binary (an atom-size ratio of 1.006) to senary (a ratio of 1.074) alloys, the size-dependent densities S' increases

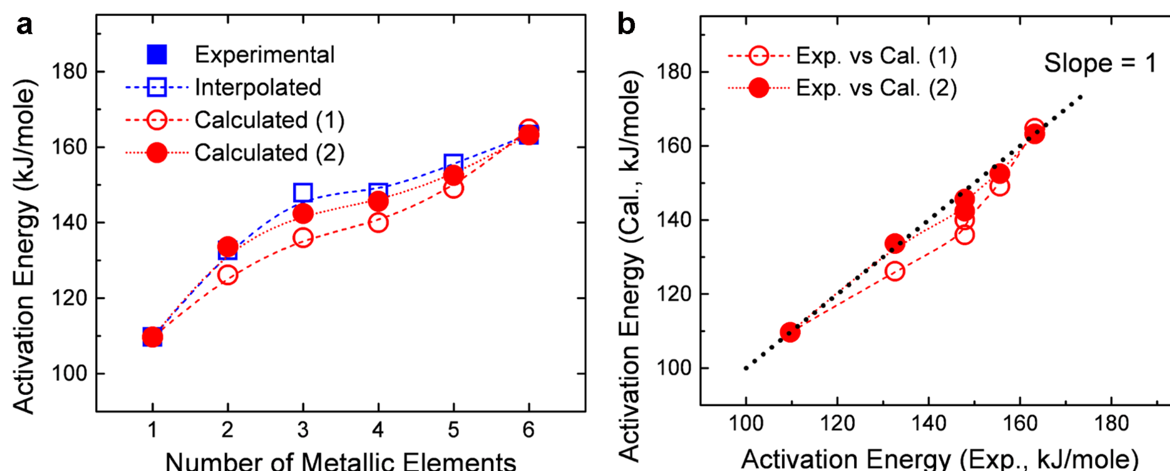

Figure 10 | (a) Experimentally measured (including interpolated) and theoretically calculated (offset) activation energy of Cu diffusion in/through *n*A alloys (*n*: number of metallic elements); (b) comparative plots w/o and w/consideration of volume-to-area transformation.

(from an original S of 0.680) to 0.683 and to 0.711, respectively. Combining the contributions of the lattice distortion strain energy, the increase in cohesive energy and the multiplied packing density, the total increases in the activation energy of diffusion in the alloys are predicted as $\Delta Q_{(1)} = \left(\Delta U_{strain} + \Delta H^{mix}\right)\frac{S'}{S}$, as plotted in Figure 9 (b). For the senary alloy, the calculated energy increase, 55 kJ/mol, nearly equals the measured increase, 53 kJ/mol (from 110 to 163 kJ/mol), suggesting the validity of the prediction.

Figure 10 comparatively presents the experimentally measured activation energy of Cu diffusion and theoretically calculated values (110 kJ/mol offset, referred to the experimental value of the unitary alloy) in the present alloys with different numbers of metallic elements. Similar trends of the experimental and calculated data with the number of metallic elements are observed though, small differences between them are found yet, possibly attributable to a "volume-to-area" effect. The reported models for Cu diffusion in alloys basically consider atom motion on a two-dimensional area[31–33]; however, the present calculations are on the basis of three-dimensional volume. By considering a volume-to-area transformation, the theoretical calculations are thus modified as $\Delta Q_{(2)} = k\left(\Delta Q_{(1)}\right)^{2/3}$ ($k \approx 3.7$), as also plotted in Figure 10. The modified calculations well match the experimental values, concluding the two-dimensional effects of the dominant three-dimensional structural (distortion/packing) and thermodynamic (cohesion) factors on the suppressed interdiffusion kinetics in the multi-component high-entropy alloys.

In summary, six solid-solution alloy barriers, from unitary Ti to senary TiTaCrZrAlRu, with different numbers of metallic elements of different atom sizes and cohesive energy were characterized. As experimentally determined, with more metallic elements added, the failure temperature of the alloy barriers against the interdiffusion of Cu and Si increased from 550 to 900°C, and the activation energy of Cu diffusion in the alloys increased from 110 to 163 kJ/mole, indicating an improved diffusion resistance of the multi-component high-entropy alloys. Mechanistically, the substitutional diffusion of Cu atoms via vacancies, with the consideration of a volume-to-area transformation, is expected. Dominate factors that provide a theoretical increase of 55 kJ/mol in the activation energy of Cu diffusion in the present multi-component alloys and suppress the interdiffusion kinetics of Cu and Si include, structurally, a high lattice distortion strain energy and a high packing density, and, thermodynamically, a high cohesive energy, to diminish the formation of vacancies and to hinder the movements of atoms, yielding an extreme diffusion resistance.

Methods

Thin and thick alloy films with different numbers of metallic elements (*n*A), including unitary Ti (1A), binary TiTa (2A), ternary TiTaCr (3A), quaternary TiTaCrZr (4A), quinary TiTaCrZrAl (5A) and senary TiTaCrZrAlRu (6A), were deposited by typical magnetron sputtering and investigated. Thin alloy diffusion barrier layers (DB_{nA}, ~7 nm) were prepared for examining their resistance to the interdiffusion of Cu and Si; thick alloy films (*n*A, 600–1000 nm) were for characterizing compositions, crystal structures and electrical resistivities. Sputtering targets were fabricated by arc-melting equimolar constituent elements in vacuum, and then cutting and polishing the solidified bulks into discs with a diameter of 50 mm. The thin barrier layers and thick alloy films were deposited on Si substrates at a radio-frequency power of 150 W and a substrate bias of −100 V, at room temperature, in an Ar atmosphere (gas flow rate of 30 sccm, working pressure of 6×10^{-3} torr). A top Cu film (50 nm) was deposited on the thin barrier layers at a power of 50 W (Ar flow rate of 13 sccm, working pressure of 5×10^{-3} torr) to form Si/DB_{nA}/Cu film stacks. Thermal annealing of the film stacks was then carried out in a tube furnace (base vacuum of 4×10^{-2} torr) at 300 to 900°C (ramping rate of 5°C/min) for 30 minutes in an N_2/H_2 atmosphere (total gas flow rate of 500 sccm, H_2 flow ratio of 5%; reducing atmosphere to prevent the film stacks from oxidation) to investigate the resistance of the barrier layers to the interdiffusion of Cu and Si. For comparison, Si/Cu without applying a diffusion barrier layer was also studied.

The elemental compositions of the thick alloy films were determined by electron probe micro-analyses (EPMA, JEOL JXA-8800M). A scanning electron microscope (SEM, JEOL JSM-6700F) was used to observe the surface morphologies of as-deposited and thermally annealed Si/DB_{nA}/Cu film stacks, and a glancing incident angle (0.5°) X-ray diffractometer (XRD, Rigaku Dmax 2000) was applied to analyze the crystal structures of the thick alloy films and the as-deposited and thermally annealed Si/DB_{nA}/Cu stacks. The sheet resistance of the thick alloy films and the film stacks was measured by using a four-point probe station (Keithley 2400) to calculate electrical resistivities. The microstructures and lattice images of the as-deposited and thermally annealed Si/DB_{nA}/Cu film stacks (with DB_{1A} and DB_{6A}) were observed by a high-resolution transmission electron microscope (TEM, JEOL JEM-2100F), and the elemental concentration profiles of Cu and Si in the film stacks were determined by line scanning analyses using energy dispersive spectrometry (EDS, Oxford).

1. Yeh, J. W. *et al.* Nanostructured high-entropy alloys with multiple principal elements: novel alloy design concepts and outcomes. *Adv. Eng. Mater.* **6**, 299–303 (2004).
2. Yeh, J. W. *et al.* Formation of simple crystal structures in Cu-Co-Ni-Cr-Al-Fe-Ti-V alloys with multi-principal metallic elements. *Metall. Mater. Trans. A* **35**, 2533–2536 (2004).
3. Yeh, J. W., Chang, S. Y., Hong, Y. D., Chen, S. K. & Lin, S. J. Anomalous decrease in X-Ray diffraction intensities of Cu-Ni-Al-Co-Cr-Fe-Si alloy systems with multi-principal elements. *Mater. Chem. Phys.* **103**, 41–46 (2007).
4. Tong, C. J. *et al.* Microstructure characterization of $Al_xCoCrCuFeNi$ high-entropy alloy system with multiprincipal elements. *Metall. Mater. Trans. A* **36**, 881–893 (2005).
5. Tong, C. J. *et al.* Mechanical performance of $Al_xCoCrCuFeNi$ high-entropy alloy system with multiprincipal elements. *Metall. Mater. Trans. A* **36**, 1263–1271 (2005).
6. Tian, F., Varga, L. K., Chen, N., Delczeg, L. & Vitos, L. Ab initio investigation of high-entropy alloys of 3d elements. *Phys. Rev. B* **87**, 075144 (2013).
7. Zhu, C., Lu, Z. P. & Nieh, T. G. Incipient plasticity and dislocation nucleation of FeCoCrNiMn high-entropy alloy. *Acta Mater.* **61**, 2993–3001 (2013).

8. Zhang, Y., Zuo, T. T., Cheng, Y. Q. & Liaw, P. K. High-entropy alloys with high saturation magnetization, electrical resistivity, and malleability. *Sci. Rep.* **3**, 1455 (2013).
9. Lai, C. H., Lin, S. J., Yeh, J. W. & Chang, S. Y. Preparation and characterization of AlCrTaTiZr multi-element nitride coatings. *Surf. Coat. Technol.* **201**, 3275–3280 (2006).
10. Chang, S. Y., Lin, S. Y., Huang, Y. C. & Wu, C. L. Mechanical properties, deformation behaviors and interface adhesion of $(AlCrTaTiZr)N_x$ multi-component coatings. *Surf. Coat. Technol.* **204**, 3307–3314 (2010).
11. Chang, S. Y., Chen, M. K. & Chen, D. S. Multiprincipal-element AlCrTaTiZr-nitride nanocomposite film of extremely high thermal stability as diffusion barrier for Cu metallization. *J. Electrochem. Soc.* **156**, G37–G42 (2009).
12. Kaloyeros, A. E. & Eisenbraun, E. Ultrathin diffusion barriers/liners for gigascale copper metallization. *Annu. Rev. Mater. Sci.* **30**, 363–385 (2000).
13. Kouno, T., Niwa, H. & Yamada, M. Effect of TiN microstructure on diffusion barrier properties in Cu metallization. *J. Electrochem. Soc.* **145**, 2164–2167 (1998).
14. Alén, P., Ritala, M., Arstila, K., Keinonen, J. & Leskelä, M. Atomic layer deposition of TaN, NbN, and MoN films for Cu metallizations. *J. Electrochem. Soc.* **152**, G361–G366 (2005).
15. Kwon, S. H., Kwon, O. K., Min, J. S. & Kang, S. W. Plasma-enhanced atomic layer deposition of Ru-Ti-N thin films for copper diffusion barrier metals. *J. Electrochem. Soc.* **153**, G578–G581 (2006).
16. Chen, C. W., Chen, J. S. & Jeng, J. S. Effectiveness of Ta addition on the performance of Ru diffusion barrier in Cu metallization. *J. Electrochem. Soc.* **155**, H438–H442 (2008).
17. Fang, J. S., Lin, J. H., Chen, B. Y. & Chin, T. S. Ultrathin Ru-Ta-C barriers for Cu metallization. *J. Electrochem. Soc.* **158**, H97–H102 (2011).
18. Leu, L. C., Norton, D. P., McElwee, L. & Anderson, T. J. Ir/TaN as a bilayer diffusion barrier for advanced Cu interconnects. *Appl. Phys. Lett.* **92**, 111917 (2008).
19. Xie, Q. *et al.* Ru thin film grown on TaN by plasma enhanced atomic layer deposition. *Thin Solid Films* **517**, 4689–4693 (2009).
20. Kim, S. H. *et al.* A bilayer diffusion barrier of ALD-Ru/ALD-TaCN for direct plating of Cu. *J. Electrochem. Soc.* **155**, H589–H594 (2008).
21. Wang, Y., Cao, F., Zhang, M. L. & Zhang, T. Property improvement of Cu-Zr alloy films with ruthenium addition for Cu metallization. *Acta Mater.* **59**, 400–404 (2011).
22. Caro, A. M. *et al.* Bottom-up engineering of subnanometer copper diffusion barriers using NH_2-derived self-assembled monolayer. *Adv. Funct. Mater.* **20**, 1125–1131 (2010).
23. Chang, S. Y. & Chen, D. S. 10-nm-thick quinary (AlCrTaTiZr)N film as effective diffusion barrier for Cu interconnects at 900°C. *Appl. Phys. Lett.* **94**, 231909 (2009).
24. Chang, S. Y., Wang, C. Y., Chen, M. K. & Li, C. E. Ru incorporation on marked enhancement of diffusion resistance of multi-component alloy barrier layers. *J. Alloy. Compd.* **509**, L85–L89 (2011).
25. Chang, S. Y. & Chen, D. S. Ultrathin (AlCrTaTiZr)Nx/AlCrTaTiZr bilayer structures with high diffusion resistance for Cu interconnects. *J. Electrochem. Soc.* **157**, G154–G159 (2010).
26. Chang, S. Y., Li, C. E., Chiang, S. C. & Huang, Y. C. 4-nm thick multilayer structure of multi-component $(AlCrRuTaTiZr)N_x$ as robust diffusion barrier for Cu interconnects. *J. Alloy. Compd.* **515**, 4–7 (2012).
27. Cheng, J. Y. & Chen, L. J. Formation of amorphous interlayers by solid-state diffusion in ultrahigh-vacuum-deposited polycrystalline Nb and Ta thin films on (111)Si. *Appl. Phys. Lett.* **58**, 45–47 (1991).
28. Wang, M. H. & Chen, L. J. Phase formation in the interfacial reactions of ultrahigh vacuum deposited titanium thin films on (111)Si. *J. Appl. Phys.* **71**, 5918–5925 (1992).
29. Yang, T. H., Chi, K. S. & Chen, L. J. Formation of Ti silicide nanocrystals in the amorphous interlayers in ultrahigh-vacuum-deposited Ti thin films on (001)Si. *J. Appl. Phys.* **98**, 034302 (2005).
30. Mehrer, H. *Diffusion in solids: fundamentals, methods, materials, diffusion-controlled processes* (Springer, Berlin, Germany, 2007).
31. Zhao, Y. & Lu, G. First-principles simulations of copper diffusion in tantalum and tantalum nitride. *Phys. Rev. B* **79**, 214101 (2009).
32. Tsetsersis, L., Logothetidis, S. & Pantelides, S. T. Migration of species in a prototype diffusion barrier: Cu, O, and H in TiN. *Appl. Phys. Lett.* **94**, 161903 (2009).
33. Tsetsersis, L., Logothetidis, S. & Pantelides, S. T. Atomic-scale mechanisms for diffusion of impurities in transition-metal nitrides. *Surf. Coat. Technol.* **204**, 2089–2094 (2010).
34. Zhang, Y., Zhou, Y. J., Lin, J. P., Chen, G. L. & Liaw, P. K. Solid-solution phase formation rules for multi-component alloys. *Adv. Eng. Mater.* **10**, 534–538 (2008).
35. Chang, S. Y., Chen, C. F., Lin, S. J. & Kattamis, T. Z. Electrical resistivity of metal matrix composites" *Acta Mater.* **51**, 6291–6302 (2003).
36. Yeh, J. W. Alloy design strategies and future trends in high-entropy alloys. *JOM* **65**, 1759–1771 (2013).
37. Miedema, A. R., de Châtel, P. F. & de Boer, F. R. Cohesion in alloys – fundamentals of a semi-empirical model. *Physica B* **100**, 1–28 (1980).
38. de Boer, F. R. & Pettifor, D. G. *Cohesion in metals: transition metal alloys* (North-Holland, Amsterdam, Netherlands, 1988).
39. Gaskell, D. R. *Introduction to the thermodynamics of materials* (5th Ed.) (Taylor & Francis, New York, NY, 2008).
40. Takeuchi, A. & Inoue, A. Quantitative evaluation of critical cooling rate for metallic glasses. Mater. *Sci. Eng. A* **304–306**, 446–451 (2001).
41. Danisch, M., Jin, Y. & Makse, H. A. Model of random packings of different size balls. *Phys. Rev. E* **81**, 051303 (2010).

Acknowledgments

The authors gratefully thank the financial supports for this research by the National Science Council, Taiwan, under Grant No. NSC-100-2628-E-005-006-MY3, and in part by the Ministry of Education, Taiwan, under the ATU plan.

Author contributions

S.Y.C. conceived of experiments, analyzed data, performed calculations, and wrote the paper. C.E.L. prepared samples and carried out characterizations. S.Y.C., Y.C.H. and H.F.H. analyzed microscopic images. S.Y.C., J.W.Y. and S.J.L. discussed results.

Additional information

Supplementary information accompanies this paper at http://www.nature.com/scientificreports

Competing financial interests: The authors declare no competing financial interests.

How to cite this article: Chang, S.-Y. *et al.* Structural and Thermodynamic Factors of Suppressed Interdiffusion Kinetics in Multi-component High-entropy Materials. *Sci. Rep.* **4**, 4162; DOI:10.1038/srep04162 (2014).

This work is licensed under a Creative Commons Attribution-NonCommercial-NoDerivs 3.0 Unported license. To view a copy of this license, visit http://creativecommons.org/licenses/by-nc-nd/3.0